PEA SYSTEM MODELING AND SIGNAL PROCESSING FOR MEASUREMENT OF VOLUME CHARGE DISTRIBUTIONS IN THIN DIELECTRIC FILMS

L. H. Pearson[(1)], J. R. Dennison[(2)], E. W. Griffiths[(1)], A. C. Pearson[(1)]

[(1)]Box Elder Innovations, LLC, 4465 W. 5900 N., Bear River City, Utah, USA, 84301, beinnov@frontier.com
[(2)]Utah State University, 4415 Old Main Hill, Logan, Utah, USA, 84322, JR.Dennison@USU.edu

ABSTRACT

This paper discusses an effort to develop advanced pulsed electroacoustic (PEA) measurement system capabilities that incorporate (1) improved signal processing tools for increased signal/noise ratios; and (2) integrated PEA modeling tools. In addition, we emphasize state-of-the-art system electronic components, integrated environmental controls, and sensor improvements required to achieve high spatial resolution while maintaining reasonable temporal resolution for both ambient and *in vacuo* measurements of thin dielectrics charged using electron beam injection, which are most applicable for spacecraft charging tests. PEA measurement systems provide an important tool to investigate the spatial extent and dynamic evolution of such embedded charge distributions in thin dielectric materials. This knowledge has important applications in spacecraft industries, as well as for semiconductors, high-power electronic devices, high-voltage DC power cable insulation, and high-energy and plasma physics apparatus. The emphasis of this paper is on improved signal processing methods and integrated PEA modeling tools.

1. APPROACH

Pulsed Electro-Acoustic (PEA) measurement techniques are nondestructive and, arguably, one of the most promising methods to provide the desired information on internal charges distributions related to spacecraft charging issues [1,2]. PEA techniques generate acoustic waves within the material by using high voltage, high frequency, pulsed signals to stimulate motion of the internal charge bound in the solid. External piezoelectric transducers convert the acoustic signal generated in this manner to an electrical signal for detection and analysis. Signal processing methods are applied to improve signal-to-noise ratios (SNR). Further, modeling tools are needed to interpret measured waveforms, to guide experimental design, and to support trouble-shooting efforts.

This work was supported by Small Business Technology Transfer Research (STTR) Phase I and Phase II funding from the Air Force Research Laboratory, Kirtland Air Force Base, Albuquerque, New Mexico, USA.

2. IMPROVED SIGNAL PROCESSING

With most raw waveform measurements, some level of signal processing has been found to be necessary in order to improve the SNR to a satisfactory level. Signal processing methods developed in this program are described below, including averaging, band-pass filter, split spectrum processing, and deconvolution. These methods are not only helpful in reducing noise, but also in improving spatial resolution.

2.1 Averaging

The most common method for improving the SNR is accomplished by simply averaging waveforms. Improvement in the SNR from averaging is proportional to the square root of the number of waveforms averaged. Hence, there is a practical limit to the use of averaging as a viable signal processing tool because of the time commitment required and the diminishing returns from averaging greater and greater numbers of waveforms. Additional signal processing tools can be applied to add additional improvement to the integrity of measured waveforms. Some of these are described below.

2.2 Band-Pass Filtering

This method applies a frequency domain Gaussian filter to the data using forward and inverse fast Fourier transforms. The frequency domain response is multiplied by a Gaussian filter which is characterized by its center frequency (f_0) and full width at half amplitude or band width (BW). The Gaussian filter is modified by a sine function to insure that it goes to zero as the frequency (f) goes to zero. The filter is given by:

$$Filter(f) = e^{-\frac{4\ln(2)}{BW^2}(f-f_0)^2} \sin\left(\frac{\pi}{2f_0} f\right). \quad (1)$$

2.3 Split Spectrum Processing (SSP)

This method was developed to reduce noise and clutter in ultrasonic waveforms coming from grain scatter in nondestructive testing of metals or other heterogeneous materials with microstructure that

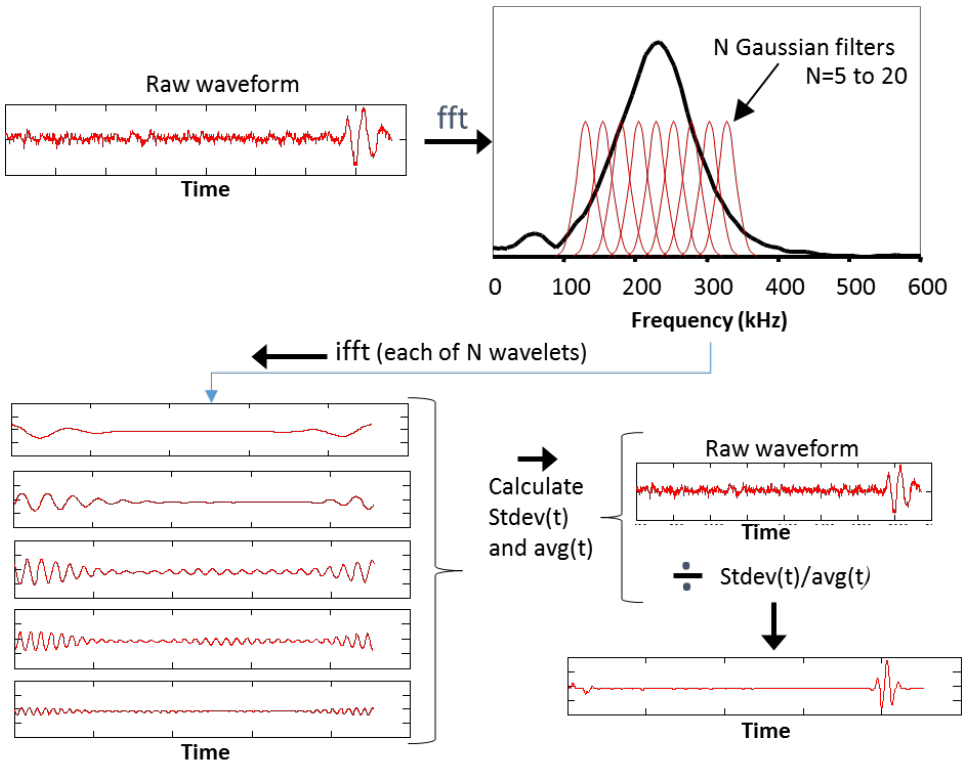

Figure 1. Graphical representation of split spectrum processing method

causes scattering [3]. SSP also works well to suppress random electronic noise in ultrasonic signals. The method contains the following steps:

(i) The raw waveform is Fourier transformed into frequency-domain and split into N wavelets using overlapping Gaussian band-pass filters.
(ii) Wavelets are transformed back into time-domain.
(iii) At each time step or element in the wavelets, the average value and standard deviation is calculated from which the coefficient of variation (CV=stdev/avg) is calculated.
(iv) The original waveform is divided at each time element by the corresponding CV.

The result is that in regions where there is a coherent signal, the CV is small and the signal is increased. In regions where noise dominates, the CV is large and the signal is reduced. Fig. 1 graphically shows this process.

2.4 Deconvolution

This method is not only for improving SNR, but also for eliminating the effects of the instrumentation/sensor response function from the waveform. Deconvolution amounts to dividing out this response in frequency-domain. The measured waveform is a convolution of the instrument response function, *h(t)*, the material response function (what we want), *x(t)*, plus noise, *n(t)*, expressed by:

$$y(t) = h(t) * x(t) + n(t) \quad . \tag{2}$$

In frequency-domain, this expression is written:

$$Y(\omega) = H(\omega)X(\omega) + N(\omega) \quad , \tag{3}$$

where each function is the Fourier transform of its time-domain counterpart. A workable solution to Eq. 41 is giving by the Wiener deconvolution [4] which is mathematically expressed as

$$X(\omega) = \frac{Y(\omega)H^*(\omega)}{|H(\omega)|^2 + Q^2|H(\omega)|^2_{\max}} \quad , \tag{4}$$

where the expression $Q^2|H(\omega)|^2_{\max}$ is a measure of the noise. Q is an adjustable parameter. Deconvolution is the final step in converting the waveform into a signal that has the shape of the charge distribution.

In summary, Fig. 2 shows the signal processing and data analysis process going from a raw waveform to a charge distribution and also shows electric and potential field calculations. The waveform is from a

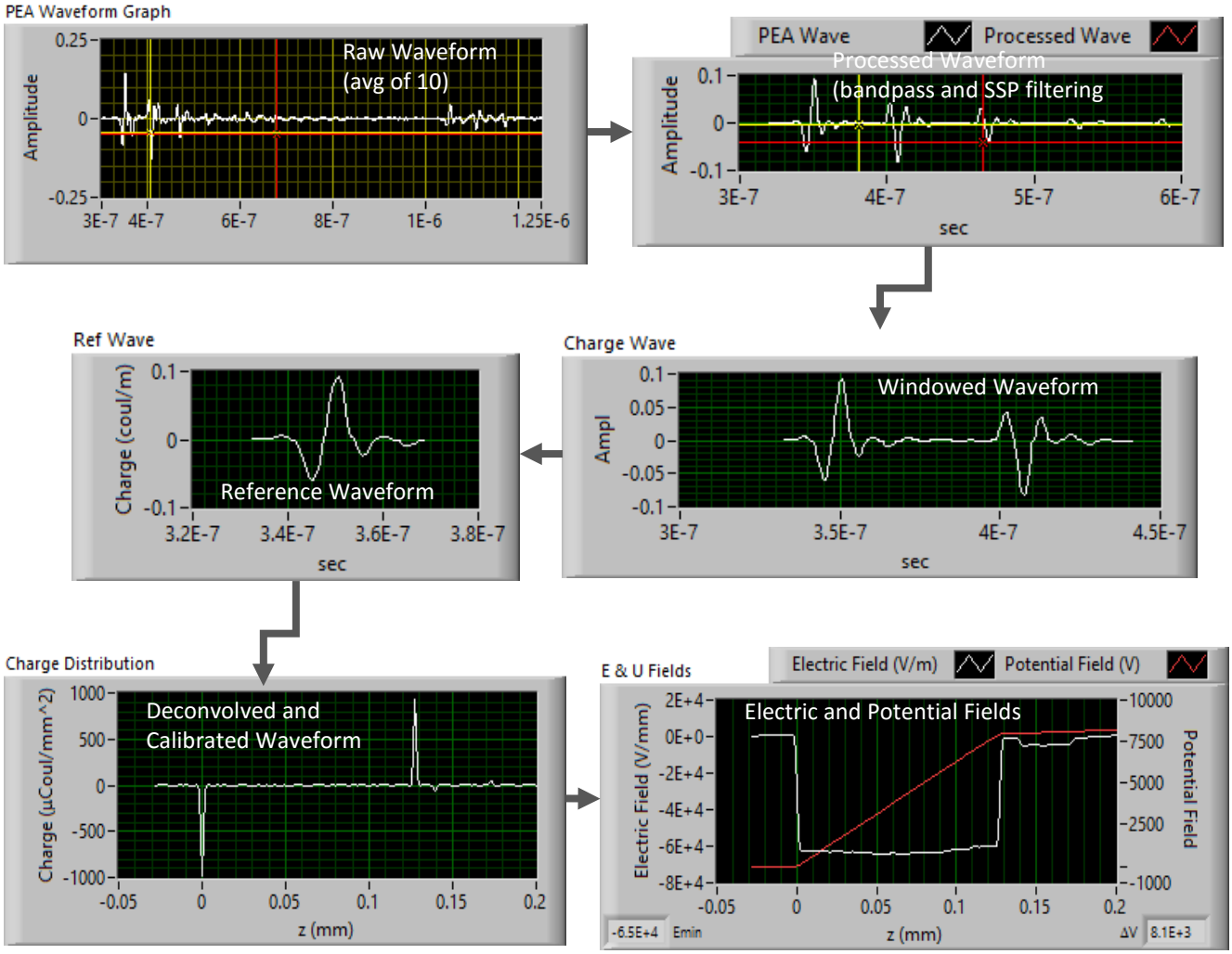

Figure 2. Flow diagram showing signal processing and data analysis process

125 μm thick polyimide (Kapton HN™) sample with no embedded charge, with 8 kV DC applied across the electrodes, and a 0.5 nsec wide excitation pulse.

3. INTEGRATED PEA MODEL

This modeling is helpful in determining the effects and relative importance of the physical parameters that are inputs to the model (*e.g.*, acoustic properties, material thicknesses, density, etc.). It also gives insight into modifications to the PEA method which can be used to improve or better understand the method. This model, as well as many other variations [1,5-15], can be classified as ray-tracing models. That is, dominant and first arriving wavelets are individually traced through the sample and adjacent material layers in the sample holding fixture and then mathematically summed, using the principle of linear superposition, to give a complete waveform that would be equivalent to the measured waveform. Most literature models only account for the initial wavelet generated by the charge layer embedded in the dielectric film. However, there are many additional wavelets coming from the sample that contain information about the charge distribution and the acoustic properties of the material layers. Fig. 3 shows a conceptual diagram of a generic PEA test setup including (not to scale) the layered material system made up of the charged dielectric film, aluminum electrodes, and piezoelectric sensor.

A brief outline of the theoretical basis of the model is presented below. The mathematical development process for the primary ray generated from a simulated embedded charge layer is outlined and includes the following key elements:

(i) The piezoelectric sensor is used to detect the wave generated by the electric field impulse, E(t).
(ii) A negative charge layer (distribution) is embedded in the dielectric film (layer) and for

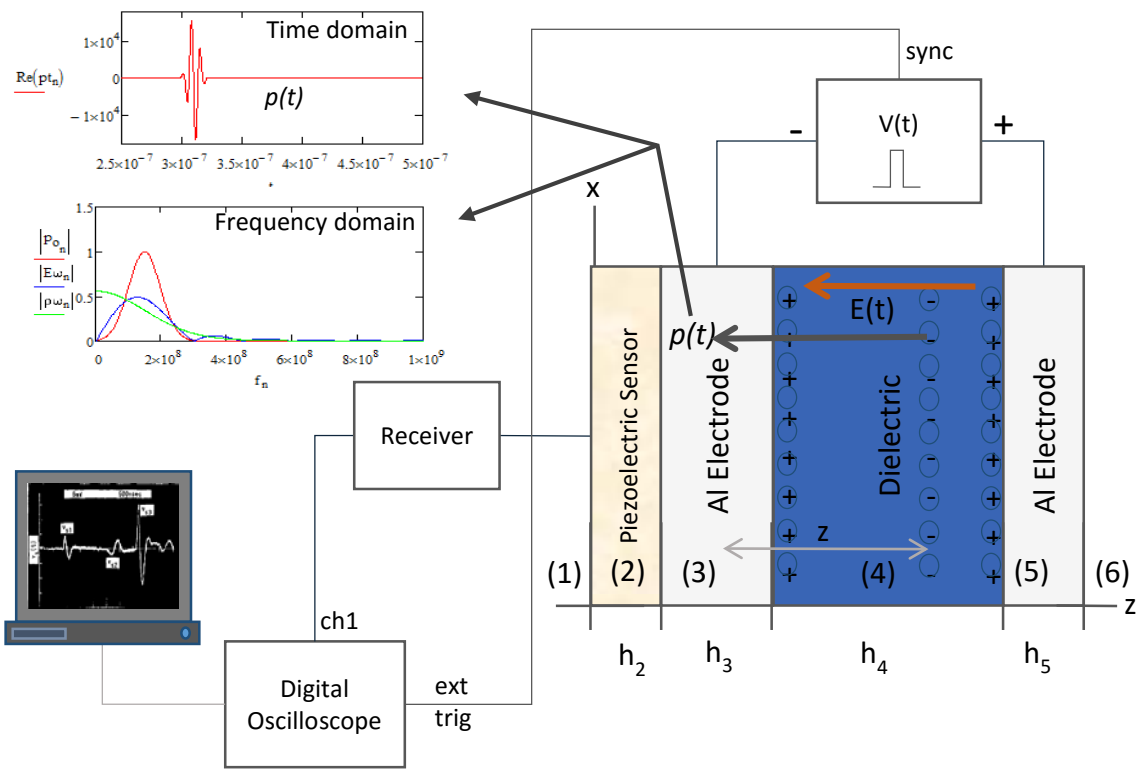

Figure 3 Conceptual diagram showing a generic PEA setup with a charged dielectric film, electrodes, sensor, and basic equipment components

simplicity, is assumed to have a shape approximated by a Maxwellian distribution function.

(iii) Charge layers are induced on the conducting electrodes on each side of the dielectric layer.

(iv) Two acoustic waves are generated by each charge layer from the force caused by *E(t)* and propagate in opposite directions from the charge layer and with opposite phase.

Constraining assumptions in the mathematical development include:

(i) The thickness of each layer is small compared to its lateral dimensions.

(ii) The lateral dimensions are large compared to the wavelength of the induced ultrasonic wave.

(iii) Assumptions (i) and (ii) lead to the assumption that there are no guided wave modes and that the problem can be treated as one-dimensional.

(iv) All acoustic waves are bulk longitudinal waves propagating normal to the plane of each layer.

(v) The charge distribution in the dielectric film only has a z-dependence (normal to the sample plane).

(vi) The aluminum electrode between the sensor and the dielectric layer is thick enough so that all multiple reflections within that layer are far enough out in time that they can be ignored.

The volume charge distribution in the dielectric layer is given by, $\rho(z)$. A force acts on the charge layer when an external pulsed electric field, $E(t)$, is applied. The force on a thin sub-layer of charge of thickness, Δz, at location z relative to the left side of the dielectric film, is given by:

$$\Delta f(z,t) = \rho(z) \cdot \Delta z \cdot E(t) \quad . \tag{5}$$

In the frequency domain, this expression can be written:

$$\Delta f(\omega, z) = \rho(z) \cdot \Delta z \cdot E(\omega) \quad , \tag{6}$$

where $\Delta f(\omega,z)$ and $E(\omega)$ are Fourier transforms of $\Delta f(z,t)$ and $E(t)$, respectively. The force (over the cross sectional area) creates a pressure wave that propagates to the piezoelectric sensor and is given by:

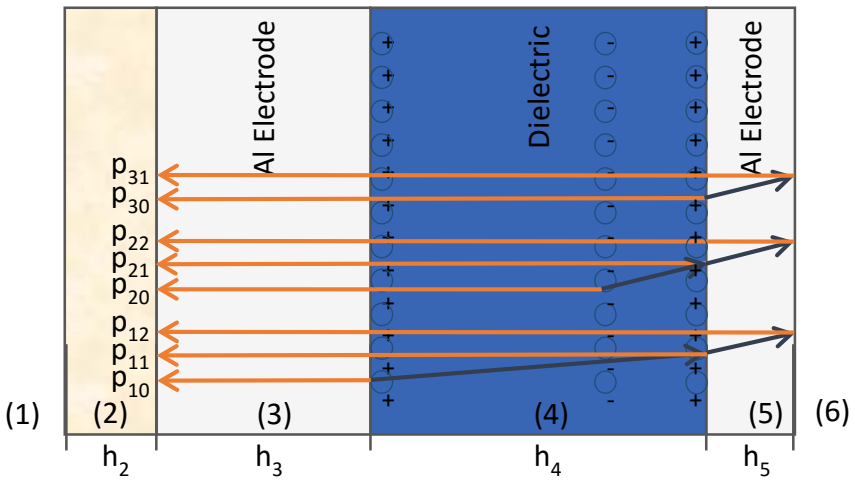

Figure 4 Drawing showing additional wavelets including additional reflecting wavelets and wavelets coming from induced charge layer

$$\Delta p(\omega, z) = p_0(\omega) \cdot \rho(z) \cdot \Delta z \cdot E(\omega) \cdot e^{ik_4 z} \cdot e^{ik_3 h_3} \cdot t_{43} \cdot t_{32} \quad (7)$$

where $p_0(\omega)$ is the transducer/instrumentation response function and is assumed, for convenience, to have a Gaussian response shape in frequency domain. t_{43} and t_{32} are the transmission coefficients for the dielectric/electrode and electrode/piezoelectric sensor interfaces, respectively (refer to Fig. 3). The exponential factors are added to account for the phase shifts (or time delays in time domain) for each respective layer. The *z*-coordinate can be transformed to a time coordinate with the following substitutions:

$$z = t \cdot c_4 \; ; \; \Delta z = c_4 \Delta t \; ; \; k_4 = \frac{\omega}{c_4} \quad , \quad (8)$$

where c_4 is the wavespeed in the dielectric, ω is the angular frequency, and k_4 is the wavevector in the dielectric. Eq. 3 can now be written as

$$\Delta p(\omega, t) = p_0(\omega) \cdot E(\omega) \cdot c_4 \cdot e^{ik_3 h_3} \cdot t_{43} \cdot t_{32} \cdot \rho(c_4 t) \cdot e^{i\omega t} \Delta t \quad (9)$$

Summing up all the wavelets from each charge sub-layer (Δz) is accomplished by integrating as follows:

$$p(\omega) = p_0(\omega) \cdot E(\omega) \cdot c_4 \cdot e^{ik_3 h_3} \cdot t_{43} \cdot t_{32} \cdot \int_0^t \rho(c_4 t) \cdot e^{i\omega t} \cdot dt \quad (10)$$

The limits on the integral can be extended to ±∞ without changing the results of the integration, because the charge is contained within the dielectric layer. The integral now becomes a Fourier integral and Eq. 10 can now be written in terms of the Fourier transform of the charge distribution, $\rho(\omega)$:

$$p(\omega) = p_0(\omega) \cdot E(\omega) \cdot c_4 \cdot e^{ik_3 h_3} \cdot t_{43} \cdot t_{32} \cdot \rho(\omega) \, . \quad (11)$$

Eq. 11 is the stress transferred to the sensor from the charge layer. The stress, σq, from the embedded charge in the dielectric layer is then given by

$$p(\omega) = E(\omega) \cdot c_4 \cdot \rho(\omega) = \sigma q \quad . \quad (12)$$

Mathematically, the time delay (phase shift) due to the *z*-dependence of the charge distribution integrates to $\rho(\omega)$, so a complex phase factor (exponential) is no longer explicit in the expression for the wave packet, $p(\omega)$. The time-domain waveform (shown in Fig. 3) is obtained by performing an inverse Fourier transform on $p(\omega)$ from Eq. 12 and then taking the real-part:

$$p(t) = \mathrm{Re}\left[icfft\left[p(\omega)\right]\right] \quad (13)$$

where *icfft* represents an inverse, complex, fast Fourier transform. Eq. 13 represents the forward calculation model and contains only the primary wavelet created from the charge layer, which transmits directly from the embedded charge layer to the sensor and does not contain any multiple reflections/transmissions. A calculated waveform is shown in Fig. 3. To obtain the charge distribution, Eq. 11 is solved for $\rho(\omega)$ yielding

$$\rho(\omega) = \frac{p(\omega) \cdot e^{-ik_3 h_3}}{p_0(\omega) \cdot E(\omega) \cdot c_4 \cdot t_{43} \cdot t_{32}} \quad (14)$$

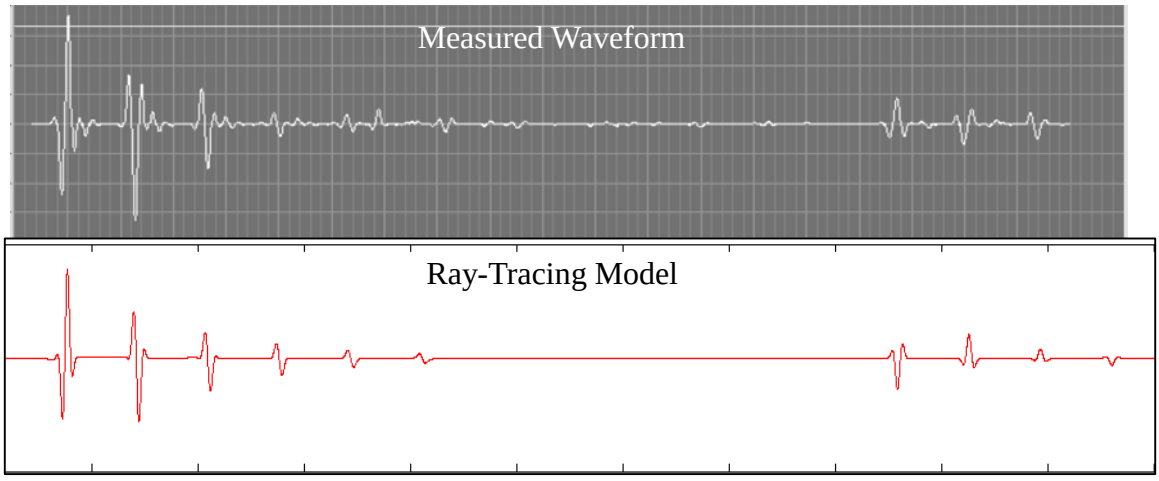

Figure 5. Comparison of measured waveform and model calculation.

This result is inverse Fourier transformed to obtain $\rho(t)$. Eq. 14 represents a deconvolution process for obtaining $\rho(\omega)$ and this result is transformed to $\rho(z)$ by using Eq. 8. The calculated frequency domain components, $p_0(\omega)$, $E(\omega)$, and $\rho(\omega)$ are also shown in Fig. 3. $P_0(\omega)$ is calculated assuming a Gaussian frequency response function for the electronic components, $E(\omega)$ is calculated assuming a half-cycle square wave pulse, or a one-cycle tone burst, and $\rho(\omega)$ is computed from Eq. 14.

Actual measured PEA waveforms show additional waves existing in the total "wave train" that come from the sample and other layers. These originate from multiple reflections and transmissions, and waves coming from the induced charge layers at the electrode/dielectric film interfaces. Graphically, some of these other waves are shown in Fig. 4. Assuming the principle of linear superposition, the total waveform can be obtained by summing all potential waves. Each wave must have an explicit mathematical expression in order to complete the sum. The derivation leading to Eqs. 11-13 is for the wave designated by p_{20} in Fig. 4. The wavelets p_{10} and p_{30}, for the waves generated from the induced charges on the electrodes, for example, can be written as:

$$p_{10}(\omega) = p_0(\omega) \cdot E(\omega) \cdot e^{ik_3 h_3} \cdot t_{32} \qquad (15)$$

$$p_{30}(\omega) = p_0(\omega) \cdot E(\omega) \cdot c_4 \cdot \rho(c_4\omega) \cdot e^{ik_3 h_3} \cdot t_{43} \cdot t_{32} \qquad (16)$$

Additional wavelets, shown in Fig. 4, can be similarly written. In theory, there are an infinite number of these addition wavelets, but in practice, only a small number of them are needed to represent the measured waveform.

4. SUMMARY

The model presented above computes the waveform, first in frequency domain; by then performing an inverse Fourier transform, the time-domain waveform is obtained. Analyzing computational results in both time domain and frequency domain yields the following observations:

(i) If $E(t)$ is a half-cycle square wave, which is commonly used in the PEA method, the theory predicts the generation of waves on both the leading and trailing edges of this signal. These waves are out of phase by 180°.
(ii) The Fourier transform of a half-cycle square wave (as is commonly used) produces a sinc function centered at zero Hz. The piezoelectric sensor frequency response, on the other hand, is centered at its natural resonant frequency and has a response that tends to zero at zero Hz. Overlaying these two responses leads one to the conclusion that much of the energy transferred into the ultrasonic wave by the electric field impulse is filtered out by the sensor. (See the frequency domain plot in Fig. 3)
(iii) It may be better for $E(t)$ to be a one-cycle toneburst with center frequency equal to the piezoelectric sensor center frequency.
(iv) The broader the bandwidth of the sensor, the narrower the time domain response and therefore, the higher the spatial resolution.

A benefit of using a ray-tracing model is that individual waves (rays) can be included or not in the calculation. This convenience makes it easy to

determine where each wave component, or wavelet, actually comes from and the route it took. This is helpful in understanding measured waveforms.

Fig. 5 gives a comparison of the ray-tracing model and a PEA measurement for a material system containing sensor backing, PVDF sensor, Al electrode, 125 μm thick polyimide dielectric film with no embedded charge, and Al electrode (see Fig. 3). The real PEA material system contains bonding layers which introduce closely spaced multiple reflections after many of the major peaks in the waveform as seen in the measurement. Some differences between model calculations and the measurement are most likely due to the estimated values for the attenuation coefficients and possible differences in the densities and wavespeeds from actual materials. Many of these properties needed for the model, especially the attenuation coefficient, are not readily available and must be measured.

In summary, signal processing and modeling tools have been developed, debugged, and proven out; they have been found to be beneficial in improving waveforms and analyzing their meaning and content.

5. REFERENCES

1. Arnaout, M., Berquez, L., Baudoin, F., and Payan, D., (2010). Contribution to Improving the Spatial Resolution of a Pulsed Electro Acoustic Cell Measurement, *IEEE Int. Conf. Solid Dielectrics*, Germany.
2. Dennison, J.R. & Pearson, L.H. "Pulse Electro-Acoustic (PEA) Measurements of Embedded Charge Distributions," (2013). *Proc. SPIE Optics and Photonics Conf.*, 8876, 887612-1-887612-11.
3. Newhouse, V.L., et.al., (1982). Flaw-to-Grain Echo Enhancement by Split-Spectrum Processing, *Ultrasonics*, Mar, p. 59.
4. Honarvar, F., et.al., (2004). A New Signal Processing Technique for Enhancement of Ultrasonic Testing Signals, *Proceedings of the World Conference on NDT*, Montreal, Canada.
5. Griseri, V., *et. al.*, (2004). Pulsed Electro-Acoustic Technique Applied to *In-situ* Measurement of Charge Distribution in Electron-irradiated Polymers, *IEEE Trans. Dielectrics and Electrical Insulation*, 11(5), 891.
6. Laurenceau, P., Dreyfus, G., and Lewiner, J., (1977). New Principle for the Determination of Potential in Dielectrics, *Phys. Rev. Lett*. 38(1), 46.
7. Sessler, G. M., West, J. E., Berkley, D. A., and Morgenster, G., (1977). Determination of Spatial Distribution of Charges in Thin Dielectrics, *Phys. Rev. Lett*. 38(7), 368.
8. Gallot-Lavallée, O., Griseri, V., Teyssedre, G., and Laurent, C., (2005). The Pulsed Electro-Acoustic Technique in Research on Dielectrics for Electrical Engineering: Today's Achievements and Perspectives for the Future, *RS - RIGE*. 8(5-6), 749.
9. Griseri, V., Bouchareb, S., Berquez, L., (2012). Adaptation of the LIMM Technique Data Treatment to Perform Measurements in Vacuum, *2012 IEEE Conference on Electrical Insulation and Dielectric Phenomena (CEIDP)*, Montreal, Quebec, Canada, October 14-17.
10. Miyake, H., Numata, S., Tanaka, Y., and Takada, T., (2010). Characteristic of Internal Charge Distribution in PI Irradiated by Proton, *10th Spacecraft Charging Tech. Conf.*, Albuquerque, NM.
11. Griseri, V., *et. al.*, (2006). Space-Charge Detection and Behavior Analysis in Electron-irradiated Polymers, *IEEE Trans. Plasma Sci.*, 34(5), 2185.
12. Maeno, T., *et. al.*, (1988). Measurement of Spatial Charge Distribution in Thick Dielectrics Using the Pulsed Electroacoustic Method, *IEEE Trans. Electrical Insulation*, 23(3), 433.
13. Takada, T., et.al., (1998). Comparison Between the PEA Method and the PWP Method for Space Charge Measurement in Solid Dielectrics, *IEEE Trans. On Dielectrics and Electrical Ins.*, 5(6), 944.
14. Takada, T., Miyake, H., and Tanaka, Y., (2006). Pulse Acoustic Technology for Measurement of Charge Distribution in Dielectric Materials for Spacecraft, *IEEE Transactions on Plasma Science*, 34(5), 2176.
15. Tashima, D., Kurosawatsu, K., Sung, Y-M., Otsubo, M., and Honda, C., (2007). Surface Modification of Nanoporous Materials for Electric Double Layer Capacitors Application, *Materials Chemistry and Physics*, 103(1), 158.